Hybrid Active-Flux and Arbitrary Injection Position Sensorless Control of Reluctance Synchronous Machines

Francois J. W. Barnard, Wikus Theo Villet, and Maarten J. Kamper, *Senior Member, IEEE*

***Abstract*—A new hybrid position sensorless control method for reluctance synchronous machine drives is presented in this paper. The active-flux (AF) and arbitrary injection position estimation techniques are combined for the first time in this hybrid controller. The controller switches between estimation techniques depending on speed and load. A hysteresis region is implemented with phase-locked loop synchronization for dynamic and stable changeovers between estimators. Implementation of the AF method at high loads allows for extended sensorless torque capabilities at high speed.**

***Index Terms*—Hybrid controller, position sensorless control (PSC), reluctance synchronous machine (RSM) drives.**

NOMENCLATURE

Symbols:

v, i, ψ	Voltage, current, and flux linkage.
R, L, Y	Resistance, inductance, and inverse inductance.
τ, p, γ	Torque, pole pairs, and current angle.
θ, n	Rotor angle, rotor speed.

Indices:

s, r	Stator, rotor.
e, m, a	Electrical, mechanical, and active.
d, q	Direct and quadrature axis.
α, β	Alpha and beta axis.

Vector quantities are represented in lowercase boldface fonts (e.g., $\boldsymbol{v}$) whereas uppercase boldface fonts represent matrices or tensors (e.g., $\mathbf{T}$). Hatted quantities denote an estimated value (e.g., $\hat{\theta}$). Subscripts describe the position of a physical quantity (e.g., stator voltage $\boldsymbol{v}_s$) or its nature (e.g., electrical angle θ_e) and superscripts the reference frame used (e.g., stator voltage in stator (α/β) reference frame $\boldsymbol{v}_s^s$).

Vector transformation from the rotor reference frame $(d{-}q)$ to the stator reference frame $(\alpha{-}\beta)$ are done using $\mathbf{T}$, whereas transformation from the stator reference frame to the rotor reference frame are done using $\mathbf{T}^{-1}$ which are, respectively, defined as

$$\mathbf{T} = \begin{bmatrix} \cos\theta_e & -\sin\theta_e \\ \sin\theta_e & \cos\theta_e \end{bmatrix} \tag{1}$$

$$\mathbf{T}^{-1} = \mathbf{T}^T. \tag{2}$$

I. INTRODUCTION

In recent years, the search for high-efficiency permanent-magnet-less motor drives has led to considerable attention being paid to the reluctance synchronous machine (RSM) [1].

RSMs have notable application possibilities in the fields of multigear electrical drives [2], high-speed geared wind generator systems [3], and particularly, industrial drives [4]. Efficient control of the RSM (using field-oriented control [5]) requires rotor position information, which is conventionally supplied by a hardware sensor. These sensors are typically unreliable and expensive compared with the rest of lower power drive systems, increasing overall cost. This motivates the use of rotor position estimation.

Estimation techniques are mainly divided into fundamental model/back electromotive force (back-EMF) schemes, and saliency-based signal injection methods. Fundamental model techniques [6]–[8] make use of flux/inductance estimation by means of a machine model or back-EMF measurement. These methods perform reliably at higher speeds but fail at low speeds. Saliency-based methods [9]–[13] exploit the angular-separated difference in rotor inductance for position estimation by means of signal excitation. These methods are able to track the rotor angle even at standstill but have limited torque capabilities because of the injected signal voltage and disappearing saliency at higher speed. Considering the capabilities of the various estimation methods, it is evident that, with their combination, as in [14]–[17], position information with full torque capabilities in the entire speed range is attainable.

A hybrid position sensorless control (PSC) scheme based on the active-flux (AF) and arbitrary injection (AI)-based methods presented in [15] and [11], respectively, is presented in this paper. It was found that the typical hybrid controller approach of using the different estimation schemes in certain speed

Manuscript received August 18, 2014; revised November 26, 2014 and January 29, 2015; accepted April 2, 2015. Date of publication April 23, 2015; date of current version September 16, 2015. Paper 2014-IDC-0578.R2, presented at the 2014 International Symposium on Power Electronics, Electrical Drives, Automation and Motion, Ischia, Italy, June 18–20, and approved for publication in the IEEE TRANSACTIONS ON INDUSTRY APPLICATIONS by the Industrial Drives Committee of the IEEE Industry Applications Society. This work was supported by the National Research Foundation of South Africa.

The authors are with the Department of Electrical and Electronic Engineering, Stellenbosch University, Stellenbosch 7602, South Africa (e-mail: fjwbarnard@gmail.com; wtvillet@gmail.com; kamper@sun.ac.za).

Color versions of one or more of the figures in this paper are available online at http://ieeexplore.ieee.org.

Digital Object Identifier 10.1109/TIA.2015.2425802

0093-9994 © 2015 IEEE. Personal use is permitted, but republication/redistribution requires IEEE permission.
See http://www.ieee.org/publications_standards/publications/rights/index.html for more information.

ranges was not viable in this case because of the AF and AI specific current requirements for producing AF (d-axis current) and having a large enough saliency (q-axis current). Constant current angle control is implemented for maximum torque per ampere (MTPA) (close to maximum efficiency), implying variable d-axis current. The AI method is parameter insensitive and requires a smaller injection voltage than other saliency-based methods, allowing extended torque capabilities. In comparison with other saliency-based techniques such as those presented in [9], which require an accurate model of the machine inductance, the AI scheme can be implemented without prior knowledge of any machine parameters. Subsequently, a novel speed-and-load-dependent scheme was derived, which implements the AF method in the higher speed and high-load range, where the AI scheme has limited torque capabilities, and AI elsewhere. The combination of these two methods also allows the possible application of this hybrid controller to any synchronous machine.

In order to further highlight the novelty of the work presented, some points should be considered. The AF method is implemented on a transverse-laminated (TL) RSM, with punched rotor flux barriers, in this paper for the first time (as opposed to the axially laminated anisotropic (ALA) RSM used in [15]). This creates a number of challenges because the TL RSM does not exhibit no-load saliency as is the case with the ALA RSM, which allows that control scheme to implement constant d-axis current (with corresponding "constant" d-axis flux-linkage) in combination with a saliency-based technique at low speeds and standstill. In addition, the ALA RSM exhibits a very predictable q-axis inductance. The TL RSM is considered to have much better potential for large-scale industrial implementation because of the simplicity of its manufacturing [4]. An interior permanent-magnet synchronous machine (which also exhibits saliency without the presence of current) is used in [8], allowing constant d-axis current for AF. Finally, the fundamental saliency technique used in [17] (for higher speeds) requires the presence of q-axis current, coinciding with the high-frequency injection technique used. Therefore, the fundamental model technique can be implemented down to a zero reference current in the higher speed region for that control scheme.

II. RSM Model

A. Mathematical Model

The motor voltage equation in stator and rotor reference frames are equal to, respectively, the following:

$$\boldsymbol{v}_s^s = R_s\boldsymbol{i}_s^s + \frac{d}{dt}\boldsymbol{\psi}_s^s \tag{3}$$

$$\boldsymbol{v}_s^r = R_s\boldsymbol{i}_s^r + \frac{d}{dt}\boldsymbol{\psi}_s^r + j\omega_e\boldsymbol{\psi}_s^r \tag{4}$$

where $\boldsymbol{v}_s^s = v_\alpha + jv_\beta, \boldsymbol{v}_s^r = v_d + jv_q$, and $\boldsymbol{v}_s^s = \mathbf{T}\boldsymbol{v}_s^r$.

Assuming a linear dependence of flux linkage on stator current in the rotor reference frame results in the following [18]:

$$\boldsymbol{\psi}_s^r = \boldsymbol{L}_s^r\boldsymbol{i}_s^r \tag{5}$$

$$\boldsymbol{\psi}_s^s = \mathbf{T}\boldsymbol{L}_s^r\mathbf{T}^{-1}\boldsymbol{i}_s^s. \tag{6}$$

TABLE I
Rated RSM Drive Parameters

Parameter	Value
Nominal Power	1.1 kW
Phase Current	3.54 A (RMS)
Rated mechanical speed (n_m)	1500 r/min*
Stator Phase Resistance (R_s)	5 Ω
Pole Pairs (p)	2
Current Angle (γ)	60°

* Reduced to 1300 r/min due to low DC link voltage.

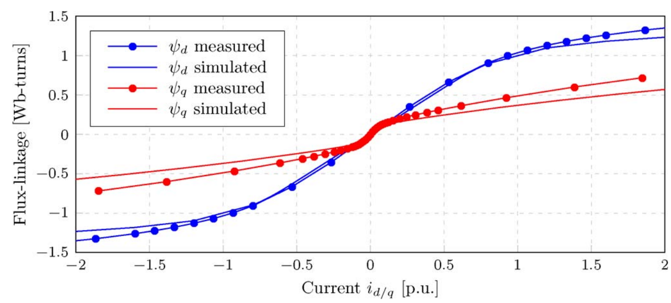

Fig. 1. Flux linkage versus p.u. d/q-current at rated current angle.

The electromechanical torque τ produced by the machine is expressed as

$$\tau = \frac{3}{2}p(L_d - L_q)i_di_q \tag{7}$$

where L is the linearized inductance $L = \psi/i$.

B. Parameters

The parameters of the RSM used in the evaluation of the presented hybrid control scheme are listed in Table I. The rated speed is lowered from 1500 to 1300 r/min because of a limited dc-link voltage (resulting from a limited 3-ϕ supply), which causes the space-vector pulsewidth modulation (SVPWM) scheme to saturate and not apply the reference voltage vector. This causes the AF estimator to fail because it is dependent on the reference voltage vector in its determination of the electrical rotor angle. The base value for the machine speed is $n_m = 1300$ r/min $= 1$ p.u.

When the machine is rotating above an appropriate speed and the load current is above 0.4 p.u. (where the d/q p.u. quantities are relative to their rated current values at rated current angle, i.e., $i_{d/q} = 1$ p.u. are $i_d = 2.5$ A & $i_q = 4.33$ A with $|\boldsymbol{i}_s| = 5$ A,$\gamma = 60°$), the estimation is done using the AF method. Fig. 1 shows that this allows for at least 50% of the flux linkage at rated current to be present, which was found to be sufficient for estimation. Note that the method presented in [15] implemented constant field current control (using rated d-current up to base speed), which is less efficient.

The linearized and tangential ($\tilde{L}_s^r$) machine inductance values in the rotor reference frame are shown in Fig. 2, as determined by finite-element model (FEM) analysis. From this figure, it is evident that, at zero current, the saliency ratio

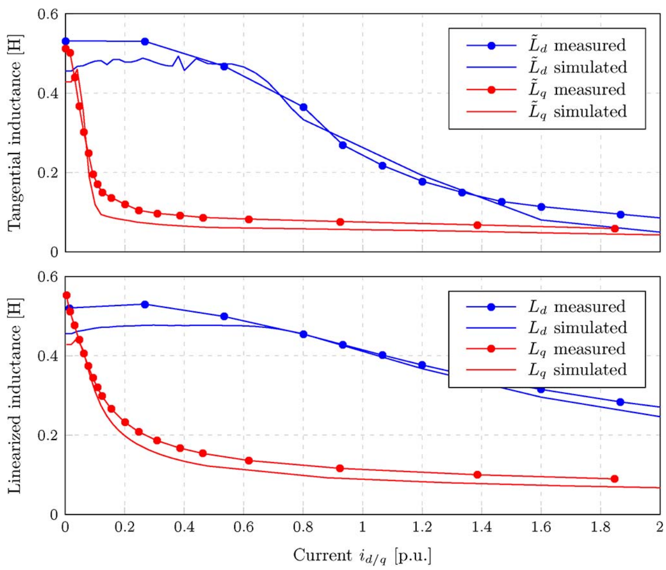

Fig. 2. Tangential and Linearized inductance versus p.u. d/q-current.

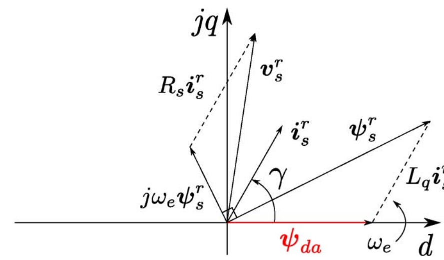

Fig. 3. Steady-state AF vector diagram in d/q-reference frame.

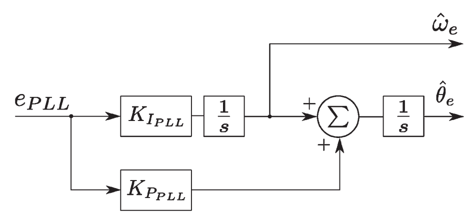

Fig. 4. PLL observer scheme with error signal input and estimation output.

$(\tilde{L_d} - \tilde{L_q})/2$ is small, which does not allow for position tracking using a saliency-based signal injection method such as AI. Therefore, a reference saturation current of at least $i_q = 0.35$ p.u. is used in this case, above which constant current angle control is implemented to ensure close to maximum efficiency (MTPA) [19].

In Fig. 2, it is shown that the q-axis inductance L_q of the evaluated RSM is notably variable with change in current and cannot be used as a constant, as is done in [15], although the AF estimator is only in control when $i_q \geq 0.4$ p.u. Consequently, inductance L_q is determined every switching cycle by means of a flux linkage lookup table. This compensates for cross-magnetization effects as well.

The flux-linkage and inductance plots in Figs. 1 and 2 show FEM computer simulated and measured results of the machine. The differences between measured and simulated results are mainly attributed to uncertainty around the actual steel used in the machine stator construction.

III. AF-Based Estimator

The AF fundamental model estimation scheme used is relatively simple and has approximately the same estimation structure for all ac machines. It turns the RSM into a fictitious nonsalient-pole (isotropic) machine with the torque given as [15]

$$\tau = \frac{3}{2} p \psi_{da} i_q \tag{8}$$

where $\psi_{da} = (L_d - L_q) i_d$ [see (7)] is the AF. The AF observer in the stator reference frame is defined as [7]

$$\hat{\boldsymbol{\psi}}_{da}^s = \int (\boldsymbol{v}_s^s - R_s \boldsymbol{i}_s^s + \boldsymbol{v}_{\text{comp}})\, dt - L_q \boldsymbol{i}_s^s \tag{9}$$

$$= \psi_{da} \cos\theta_{\psi_{da}} + j\psi_{da} \sin\theta_{\psi_{da}}. \tag{10}$$

The AF concept can be graphically understood by the steady-state vector diagram shown in Fig. 3. Integrator drift is caused by parameter estimation and measurement errors [20]. This drift is rectified with a compensation voltage $\boldsymbol{v}_{\text{comp}}$, which is a function of the voltage-flux and current-flux models of the machine defined as [15]

$$\boldsymbol{\psi}_{sv}^s = \int (\boldsymbol{v}_s^s - R_s \boldsymbol{i}_s^s + \boldsymbol{v}_{\text{comp}})\, dt \tag{11}$$

$$\boldsymbol{\psi}_{si}^s = \mathbf{T}(\psi_d + j\psi_q). \tag{12}$$

By feeding the difference of the two models through a proportional–integral (PI) compensator as in (13), $\hat{\boldsymbol{\psi}}_s^s = \boldsymbol{\psi}_{sv}^s$, which is predominantly equal to the current-flux model at low frequencies and the voltage-flux model at higher frequencies [15]. This compensates for pure integrator offset and drift errors, as well as stator resistance measurement errors [15]. Subsequently, the estimated AF vector can be calculated as in

$$\boldsymbol{v}_{\text{comp}} = \left(K_P + \frac{K_I}{s}\right)(\boldsymbol{\psi}_{si}^s - \boldsymbol{\psi}_{sv}^s) \tag{13}$$

$$\hat{\boldsymbol{\psi}}_{da}^s = \hat{\boldsymbol{\psi}}_s^s - L_q \boldsymbol{i}_s^s. \tag{14}$$

The phase-locked loop (PLL)-based observer scheme shown in Fig. 4 is used for the estimator derived herein, which results in the estimated electrical angle by feeding the error signal $K \sin\theta_{\text{err}}$ in the following through a PI controller, forcing it to zero [21]. The complete AF-based estimator is shown in Fig. 5 in block diagram format

$$K \sin\theta_{\text{err}} = \psi_{da\beta} \cos\hat{\theta}_e - \psi_{da\alpha} \sin\hat{\theta}_e \tag{15}$$

$$= \left|\hat{\boldsymbol{\psi}}_{da}^s\right| \sin\left(\theta_{\hat{\psi}_{da}^s} - \hat{\theta}_e\right). \tag{16}$$

IV. AI-Based Estimator

The AI saliency-based method used is a rather novel concept relying on the presence of a current derivative with the advantage of requiring no predetermined injection signal shape,

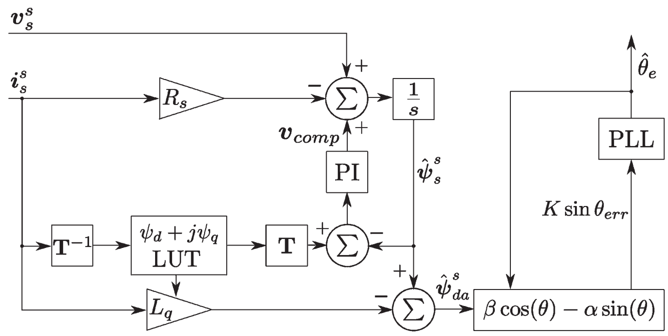

Fig. 5. AF-based estimation scheme block diagram.

allowing the use of a smaller fraction of the dc bus voltage [11]. This scheme enables elimination of some machine parameters in the position estimation algorithm and online parameter identification, allowing position estimation without any knowledge of machine parameters [22].

The flux linkage derivative is calculated with (3) and (6) as [11]

$$\frac{d\boldsymbol{\psi}_s^s}{dt} = \boldsymbol{L}_s^s \frac{d\boldsymbol{i}_s^s}{dt} + \frac{d\boldsymbol{L}_s^s}{dt}\boldsymbol{i}_s^s \tag{17}$$

with $\boldsymbol{L}_s^s = \mathbf{T}\boldsymbol{L}_s^r\mathbf{T}^{-1}$ and

$$\boldsymbol{L}_s^s = L_\Sigma \mathbf{I} + L_\Delta \mathbf{S}(\theta_e) \tag{18}$$

where

$$L_\Sigma = \frac{\tilde{L}_d + \tilde{L}_q}{2} \quad L_\Delta = \frac{\tilde{L}_d - \tilde{L}_q}{2}$$
$$\mathbf{S}(\theta_e) = \begin{bmatrix} \cos 2\theta_e & \sin 2\theta_e \\ \sin 2\theta_e & -\cos 2\theta_e \end{bmatrix}$$
$$\frac{d\boldsymbol{L}_s^s}{dt} = \frac{\partial \boldsymbol{L}_s^s}{\partial \theta_e}\omega_e.$$

Solving for the current/time derivative results in [11]

$$\frac{d\boldsymbol{i}_s^s}{dt} = \boldsymbol{L}_s^{s-1}\left(\boldsymbol{v}_s^s - R_s\boldsymbol{i}_s^s - \omega_e \frac{\partial \boldsymbol{L}_s^s}{\partial \theta_e}\boldsymbol{i}_s^s\right) \tag{19}$$

where the inverse of the inductance in the stator reference frame equals

$$\boldsymbol{L}_s^{s-1} = Y_\Sigma \mathbf{I} + Y_\Delta \mathbf{S}(\theta_e) \tag{20}$$

with inverse inductances

$$Y_\Sigma = \frac{Y_d + Y_q}{2} \quad Y_\Delta = \frac{Y_d - Y_q}{2}, Y = \frac{1}{\tilde{L}}.$$

The current progression is derived from (19) by substituting $d\boldsymbol{i}_s^s/dt = \Delta\boldsymbol{i}_s^s/\Delta t$ to result in [11]

$$\Delta\boldsymbol{i}_s^s = \tilde{\boldsymbol{L}}_s^{s-1}\left(\boldsymbol{v}_s^s - R_s\boldsymbol{i}_s^s\right)\Delta t - \omega_e \tilde{\boldsymbol{L}}_s^{s-1}\frac{\partial \tilde{\boldsymbol{L}}_s^s}{\partial \theta_e}\boldsymbol{i}_s^s\Delta t \tag{21}$$
$$= \tilde{\boldsymbol{L}}_s^{s-1}\boldsymbol{v}_L^s\Delta t + \Delta\boldsymbol{i}_{\mathrm{FM}}^s \tag{22}$$

which is separated into scaling and rotating components as

$$\Delta\boldsymbol{i}_s^s = Y_\Sigma \boldsymbol{v}_L^s \Delta t + Y_\Delta \mathbf{S}(\theta_e)\boldsymbol{v}_L^s\Delta t + \Delta\boldsymbol{i}_{\mathrm{FM}}^s \tag{23}$$
$$= \Delta\hat{\boldsymbol{i}}_{s\Sigma}^s + \Delta\boldsymbol{i}_{\mathrm{HF}}^s + \Delta\boldsymbol{i}_{\mathrm{FM}}^s. \tag{24}$$

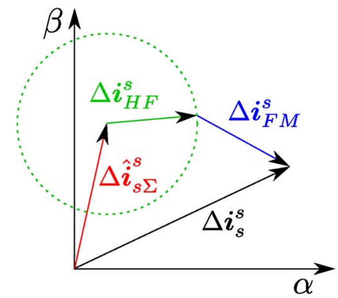

Fig. 6. AI current progression vector components.

Fig. 6 shows the actual machine current progression for AI separated into its components as in (24). Both rotating components, $\Delta\boldsymbol{i}_{\mathrm{HF}}^s$ and $\Delta\boldsymbol{i}_{\mathrm{FM}}^s$, contain rotor position information, but $\Delta\boldsymbol{i}_{\mathrm{FM}}^s$ scales with rotor speed and is thus not available at standstill.

The current progression of an isotropic machine $\Delta\hat{\boldsymbol{i}}_{s\Sigma}^s$ (with saliency consciously neglected) can be predicted from (21) by consciously neglecting the saliency ($\tilde{L}_d = \tilde{L}_q$) and using the Euler approximation as [11]

$$\Delta\hat{\boldsymbol{i}}_{s\Sigma}^s[n] = Y_\Sigma\left(\boldsymbol{v}_s^s[n_1] - R_s\boldsymbol{i}_s^s[n_1]\right)\Delta t. \tag{25}$$

$[n_1] = [n-1]$ refers to the previous calculation interval. In contrast, the measured current progression of the salient pole machine is calculated using

$$\Delta\boldsymbol{i}_s^s[n] = \boldsymbol{i}_s^s[n] - \boldsymbol{i}_s^s[n_1]. \tag{26}$$

The machine saliency is consciously neglected in (25) to be compared with the measured current progression of the anisotropic machine. The difference in progressions enable position estimation using the rotating progression components.

A. Parameter Reduction and Position Estimation

From [11], assuming that the resistive voltage vector $R_s\boldsymbol{i}_s^s$ in (25) stays constant within two switching cycles ($2\Delta t = 2t_s$), the difference between consecutive predicted current progressions can be calculated using the stator voltage as

$$\Delta\hat{\boldsymbol{i}}_{s\Sigma}^s[n_1] - \Delta\hat{\boldsymbol{i}}_{s\Sigma}^s[n_2] = Y_\Sigma\left(\boldsymbol{v}_s^s[n_1] - \boldsymbol{v}_s^s[n_2]\right)\Delta t$$
$$\Delta\left(\Delta\hat{\boldsymbol{i}}_{s\Sigma}^s\right) = Y_\Sigma\left(\Delta\boldsymbol{v}_s^s\right)\Delta t \tag{27}$$
$$\Delta\left(\Delta\boldsymbol{i}_s^s\right) = \boldsymbol{i}_s^s[n] - 2\boldsymbol{i}_s^s[n_1] + \boldsymbol{i}_s^s[n_2]. \tag{28}$$

The difference $\Delta(\Delta\boldsymbol{i}_s^s)$ refers to the measured stator current progressions [11].

The high-frequency component $\Delta\boldsymbol{i}_{\mathrm{HF}}^s$, in (30) of the difference between the measured and predicted current progressions $\boldsymbol{i}_{\Delta\mathrm{err}}^s$, in (29) is an angle-dependent term and can be predicted

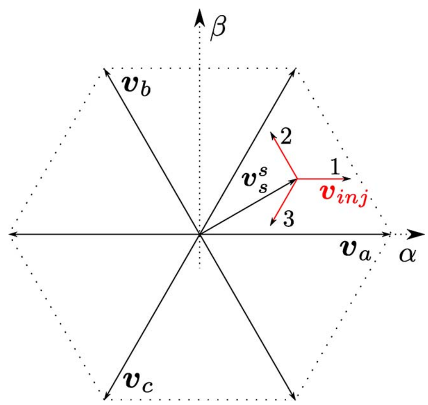

Fig. 7. Injected voltage vector diagram inside the limits of SVPWM.

using the estimated angle of a PLL according to [18] and simplified considering consecutive progressions as

$$\boldsymbol{i}_{\Delta\text{err}}^s = \Delta\left(\Delta\boldsymbol{i}_s^s\right) - \Delta\left(\Delta\hat{\boldsymbol{i}}_{s\Sigma}^s\right) \quad (29)$$

$$\Delta\boldsymbol{i}_{\text{HF}}^s = \mathbf{T}.HPF\left(\mathbf{T}^{-1}\boldsymbol{i}_{\Delta\text{err}}^s\right) \quad (30)$$

$$\Delta\hat{\boldsymbol{i}}_{\text{HF}}^s = Y_\Delta\mathbf{S}(\theta_{\text{PLL}})\left(\boldsymbol{v}_s^s - R_s\boldsymbol{i}_s^s\right)\Delta t \quad (31)$$

$$= Y_\Delta\mathbf{S}(\theta_{\text{PLL}})\Delta\boldsymbol{v}_s^s\Delta t. \quad (32)$$

Subsequently, assuming the PLL angle is correct, the vectors $\Delta\boldsymbol{i}_{\text{HF}}^s$ and $\Delta\hat{\boldsymbol{i}}_{\text{HF}}^s$ will be oriented the same way [18]. The PLL is closed by taking the error as the vector product of these vectors as [18]

$$e_{\text{PLL}} = \Delta\boldsymbol{i}_{\text{HF}}^{s\ T}\mathbf{J}\Delta\hat{\boldsymbol{i}}_{\text{HF}}^s, \quad \mathbf{J} = \mathbf{T}\left(\frac{\pi}{2}\right)$$

which will be equal to zero when $\theta_{\text{PLL}} = \theta_e$. Then, considering orientation only

$$e_{\text{PLL}} = \Delta\boldsymbol{i}_{\text{HF}}^{s\ T}\mathbf{J}\ \mathbf{S}(\theta_{\text{PLL}})\Delta\boldsymbol{v}_s^s. \quad (33)$$

This error is fed into a PLL observer scheme with the same structure as shown in Fig. 4 to result in the estimated angle and angular frequency.

B. Injection Sequence and Parameter Identification

Since this estimation scheme requires the presence of a current time derivative in the stator reference frame, a square wave spatially rotating 120° in the stator reference frame every switching cycle (t_s) is injected. This allows online admittance calculation because it is stepped in integer fractions of 360° and the high frequency yields more frequent position information, larger separation from the current controller bandwidth, and lower audible noise [11].

The injected voltage vector superimposed on the stator voltage vector is shown in Fig. 7 with the outline of the hexagon being the maximum voltage that can be applied using SVPWM.

From (27), (28), and (33), the only remaining machine parameter for position estimation is the mean admittance Y_Σ. The resulting current slope for an applied voltage vector represents the admittance for that voltage excitation. From [22], the admittance for a certain switching cycle can be calculated as

$$\hat{Y}_{tX} = \frac{\Delta\boldsymbol{i}_{\text{HF}}^{s\ T}\boldsymbol{v}_s^s}{\boldsymbol{v}_s^{s\,T}\boldsymbol{v}_s^s}, \quad X = 1, 2, 3. \quad (34)$$

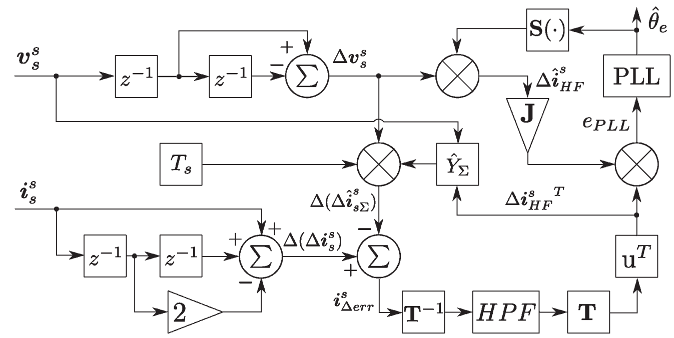

Fig. 8. AI-based estimation scheme block diagram.

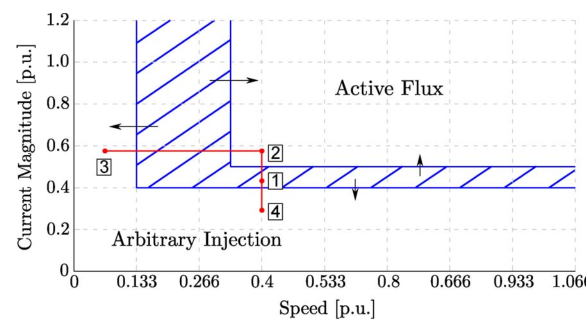

Fig. 9. Hybrid estimation scheme regions with highlighted hysteresis region and operating points for the practical tests shown in Fig. 15.

Since the injected voltages are symmetrically distributed, the mean admittance estimation equals [22]

$$\hat{Y}_\Sigma = \frac{\hat{Y}_{t1} + \hat{Y}_{t2} + \hat{Y}_{t3}}{3}. \quad (35)$$

The complete AI-based estimator is shown in Fig. 8 in a block diagram format.

V. Hybrid Controller

The new hybrid estimation scheme derived herein combines the AF and AI methods using a hysteresis approach shown in Fig. 9. The regions were chosen using the following criteria:

- at least 0.333 p.u. mechanical rotor speed to enter AF (this allows fast enough PLL synchronization);
- at least 0.133 p.u. n_m to maintain AF estimation;
- at least 0.4 p.u. d-axis saturation current
- A 0.1 p.u. current buffer for hysteresis.

Switching between estimation schemes only occurs when crossing the edges of the hysteresis region in the direction of the arrows shown. This eliminates back and forth switching between states at a certain operating point. At changeover, the PLL of the estimation scheme taking over is synchronized by setting its PLL angle equal to the current estimated angle $\theta_{\text{PLL}} = \hat{\theta}_e$ and allowing one switching cycle calculation time. The inactive estimation scheme is also kept close to synchronization using the current estimated angle. This limits large estimation differences for the estimation schemes and was found to behave in a stable manner.

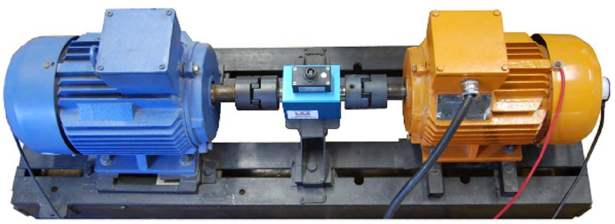

Fig. 10. Machines used for practical tests. RSM—Orange; IM—Blue.

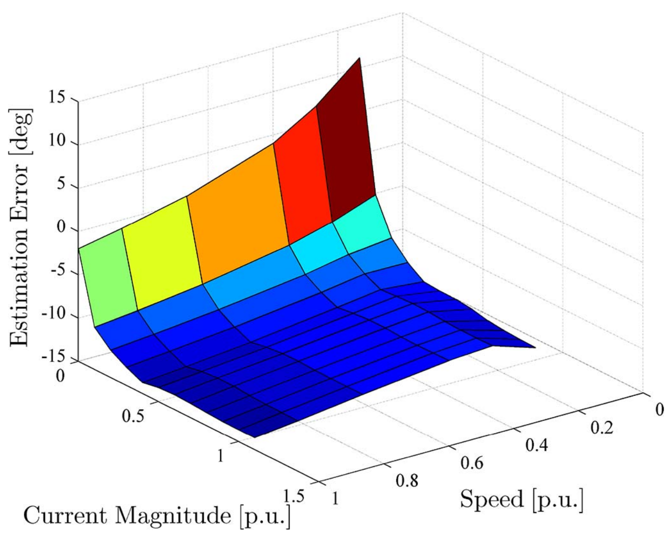

Fig. 11. Positive current (motor) error compensation map for AF plotting estimation error versus current magnitude and machine speed.

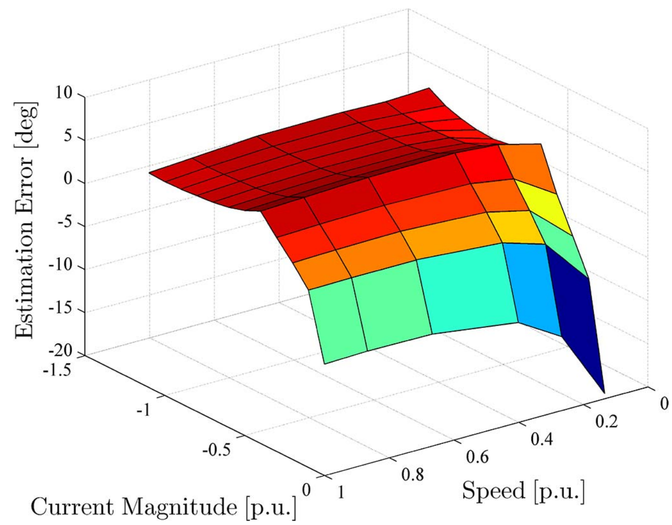

Fig. 12. Negative current (generator) error compensation map for AF plotting estimation error versus current magnitude and machine speed.

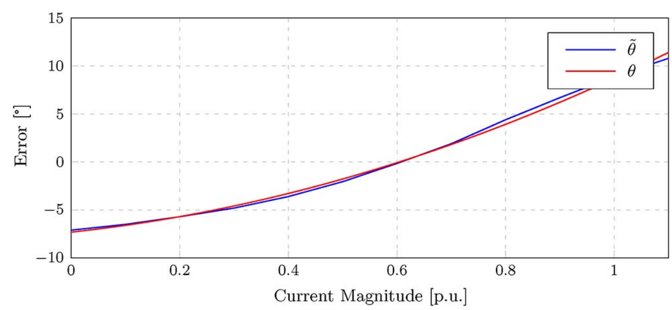

Fig. 13. Positive current estimation error with a fitted compensation curve for the AI method plotting estimation error $(\tilde{\theta})$ and compensation (θ) versus current magnitude.

Two shaft-connected machines used in the testing and evaluation of the proposed method are shown in Fig. 10. The RSM is connected via a torque sensor to an induction machine (IM). Two dc-link-connected inverters are used to drive both machines. The switching signals for the inverters are applied by two Linux-based rapid prototyping systems on which the complete control algorithm runs.

Field-oriented control is implemented on the RSM with constant current angle $\gamma = \gamma_{\mathrm{rated}}$, maintained (except at low currents for q-axis saturation) for close to maximum efficiency. This control scheme (SVPWM) applies the best combination of the eight switching vectors possible for a three-phase inverter (see Fig. 7) to reproduce the reference voltage vector. This reference voltage is the output of a current controller in rotor reference frame (d/q) for torque control (see (7)). Current measurements are done in stator reference frame (α/β) and thus have to be transformed using (2). Consequently, rotor position information is required, which is supplied by the estimation scheme and a position resolver for comparison/evaluation.

VI. Measured Results

It was found that rather strong error compensation was required for the AF method to operate as a sensorless control scheme. Figs. 11 and 12, respectively, show the positive and negative current compensation maps that were implemented for the AF method. It was found that the influence of the current-flux model $(\boldsymbol{\psi}_{si}^{s})$ on the compensation voltage $(\boldsymbol{v}_{\mathrm{comp}})$ had to be reduced in the negative current region to normalize the compensation required and enable sensorless stability. It can be seen from the figures that, above the current magnitude for d-axis saturation (0.4 p.u.), the estimation error is much less affected by speed, but it was found that speed compensation was required nonetheless.

Because of saliency shift in the machine at higher currents (see Fig. 2) error compensation is also required for the AI method. Fig. 13 shows the estimation error and second-order curve fitted compensation curve implemented for the AI method.

Fig. 14 shows an 80% load sensorless standstill to a rated speed control step of the RSM followed by an increased load step (by the IM) to about 105%. The hybrid controller starts with AI at standstill and switches to AF and back to AI at 0.333 p.u. and 0.133 p.u., respectively. This test showcases sensorless speed control in the entire rated speed and current range of the RSM.

Sensorless speed control of the RSM around the hysteresis region is shown in Fig. 15 with about 60% load applied. It can be seen that the control switches reliably between estimation schemes and that speed control is stable at the application initially and removal of the load at the end. Fig. 9 shows the operating points of this test around the hysteresis region.

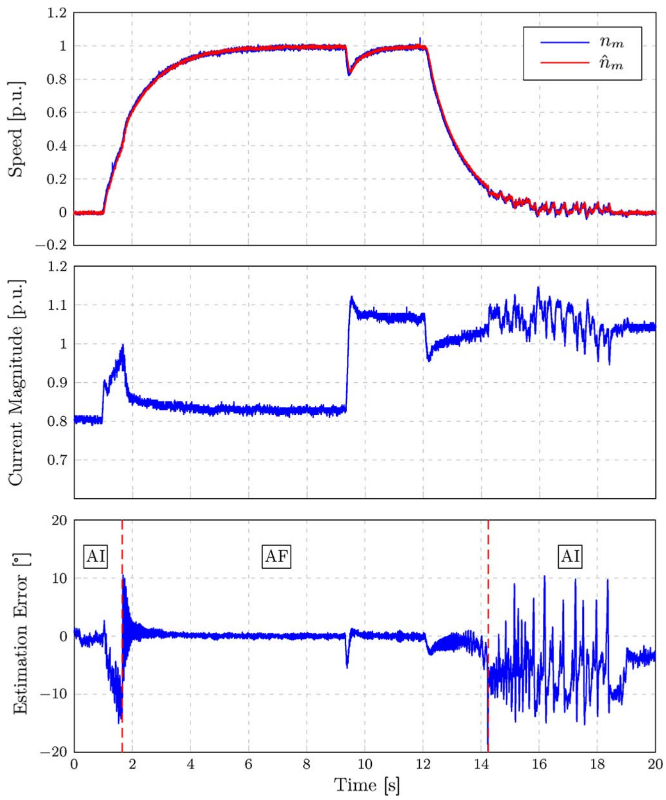

Fig. 14. Sensorless speed control at about 80% load from standstill to rated speed followed by a load step to about 105% load, showing mechanical speed, reference current, and estimated angle error versus time.

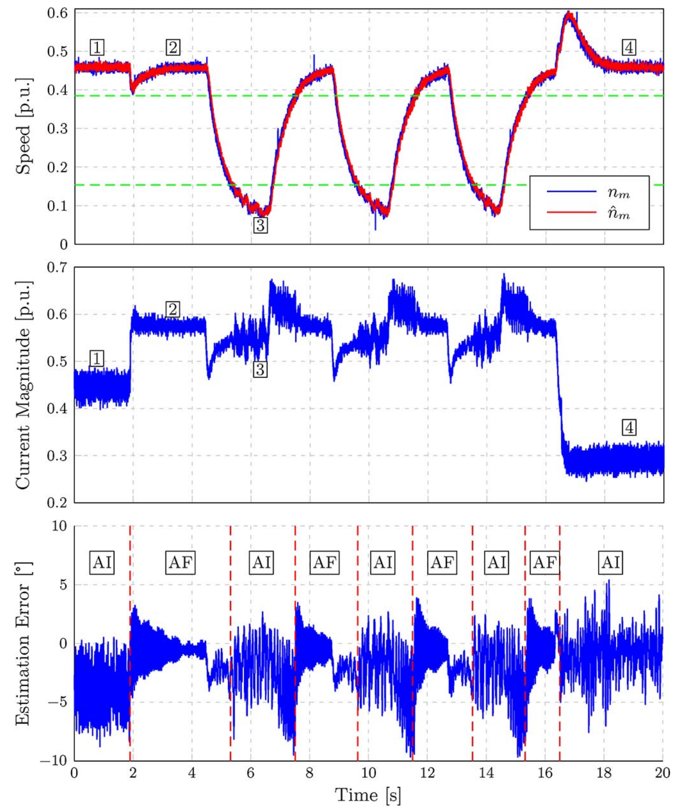

Fig. 15. Sensorless speed control with about 60% load from standstill to rated speed showing mechanical rotor speed, current amplitude, and estimated angle error versus time.

Fig. 16 shows a 20% to 100% load control step at $t \approx 29.5$ ms at rated speed. The estimated angles shown are uncompensated for load in order to show the effects thereof. This figure shows that the sensorless current control is stable with instant switchover between estimation schemes and settles within 5 ms. The measurement confirms successful sensorless control during large load transients even at high speed.

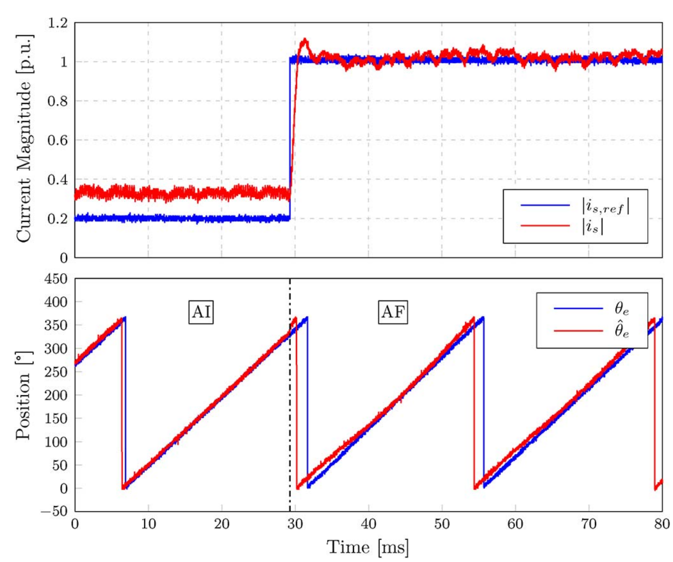

Fig. 16. 20% to 100% sensorless load control step at rated speed showing current response and uncompensated estimated angles versus time.

VII. Conclusion

In this paper, a hybrid AF plus AI position estimation scheme has been proposed and practically implemented for PSC of the RSM drive. From the research and results, the following conclusions are drawn.

- With the proposed hybrid scheme, the PSC of the RSM is demonstrated from standstill to rated speed in the entire rated load range. For the investigated 1.1-kW drive system the load control is stable and settles in about 10 ms for a large current step input crossing the changeover region.
- The AF position estimation scheme is implemented for sensorless control of a transverse laminated RSM for the first time. Significant alterations to the proposed methodology in [15] had to be implemented.
- The AI and AF estimation schemes are combined in a hybrid controller for the first time. A novel speed-and-load-dependent scheme is derived to enable close to maximum efficiency control.
- It is found that, with maximum TPA control, the AF position estimation scheme cannot be used at zero or low loads, even if the machine has good saliency because a minimum amount of d-axis current is required. This distinguishes the AF method drastically from the fundamental scheme method of [6], where a minimum amount

of q-axis current is required (which becomes very small if the saliency of the machine is good).

- With maximum TPA control, it is found that the updating AF scheme proposed by [15] cannot be used for a normal transverse laminated rotor RSM because the HFI method requires q-axis saturation current.
- It is found that the AI method can be used at rated speeds, but only at low loads because the AI estimator has a growing estimation error at higher speeds under load caused by saliency shift.
- The hybrid controller can be made more dynamic by implementing a mechanical model-based PLL for the AF method to reduce estimation errors during speed transients.

ACKNOWLEDGMENT

Opinions expressed and conclusions arrived at are those of the authors and are not necessarily to be attributed to the NRF.

REFERENCES

[1] I. Boldea, *Reluctance Synchronous Machines and Drives*, ser. Monographs in Electrical and Electronic Engineering. Oxford, U.K.: Clarendon, 1996.

[2] M. Prins, C. Vorster, and M. Kamper, "Reluctance synchronous and field intensified-pm motors for variable-gear electric vehicle drives," in *Proc. IEEE ECCE*, 2013, pp. 657–664.

[3] S. Tokunaga and K. Kesamaru, "Fem simulation of novel small wind turbine generation system with synchronous reluctance generator," in *Proc. ICEMS*, 2011, pp. 1–6.

[4] A. Vagati, "The synchronous reluctance solution: a new alternative in ac drives," in *Proc. 20th IEEE IECON*, vol. 1, 1994, pp. 1–13.

[5] T. Matsuo and T. Lipo, "Field oriented control of synchronous reluctance machine," in *Proc. 24th Annu. IEEE PESC*, 1993, pp. 425–431.

[6] P. Landsmann, R. Kennel, H. de Kock, and M. Kamper, "Fundamental saliency based encoderless control for reluctance synchronous machines," in *Proc. XIX ICEM*, 2010, pp. 1–7.

[7] I. Boldea and S. Agarlita, "The active flux concept for motion-sensorless unified ac drives: A review," in *Proc. Int. ACEMP*, 2011, pp. 1–16.

[8] A. Ejlali, S. Taravat, and J. Soleimani, "Comparative study on control strategy of dtfc based on active flux concept and dtc for ipmsm applied to traction motor," in *Proc. Int. SPEEDAM*, 2012, pp. 200–206.

[9] A. Ravikumar Setty, S. Wekhande, and K. Chatterjee, "Comparison of high frequency signal injection techniques for rotor position estimation at low speed to standstill of pmsm," in *Proc. IEEE 5th IICPE*, 2012, pp. 1–6.

[10] D. Raca, P. Garcia, D. Reigosa, F. Briz, and R. Lorenz, "A comparative analysis of pulsating versus rotating vector carrier signal injection-based sensorless control," in *Proc. 23rd APEC*, 2008, pp. 879–885.

[11] D. Paulus, P. Landsmann, and R. Kennel, "Sensorless field-oriented control for permanent magnet synchronous machines with an arbitrary injection scheme and direct angle calculation," in *Proc. Symp. SLED*, 2011, pp. 41–46.

[12] G. Andreescu and C. Schlezinger, "Enhancement sensorless control system for pmsm drives using square-wave signal injection," in *Proc. Int. SPEEDAM*, 2010, pp. 1508–1511.

[13] W. Villet, M. Kamper, P. Landsmann, and R. Kennel, "Evaluation of a simplified high frequency injection position sensorless control method for reluctance synchronous machine drives," in *Proc. 6th IET Int. Conf. PEMD*, 2012, pp. 1–6.

[14] C. Silva, G. Asher, and M. Sumner, "Hybrid rotor position observer for wide speed-range sensorless pm motor drives including zero speed," *IEEE Trans. Ind. Electron.*, vol. 53, no. 2, pp. 373–378, Apr. 2006.

[15] S.-C. Agarlita, I. Boldea, and F. Blaabjerg, "High-frequency-injection-assisted "active-flux"-based sensorless vector control of reluctance synchronous motors, with experiments from zero speed," *IEEE Trans. Ind. Appl.*, vol. 48, no. 6, pp. 1931–1939, Nov./Dec. 2012.

[16] E. Capecchi, P. Guglielmi, M. Pastorelli, and A. Vagati, "Position-sensorless control of the transverse-laminated synchronous reluctance motor," *IEEE Trans. Ind. Appl.*, vol. 37, no. 6, pp. 1768–1776, Nov./Dec. 2001.

[17] W. Villet, M. Kamper, P. Landsmann, and R. Kennel, "Hybrid position sensorless vector control of a reluctance synchronous machine through the entire speed range," in *Proc. 15th Int. EPE/PEMC*, 2012, pp. LS4b-1.1-1–LS4b-1.1-7.

[18] P. Landsmann, D. Paulus, P. Stolze, and R. Kennel, "Saliency based encoderless predictive torque control without signal injection for a reluctance synchronous machine," in *Proc. 14th Int. Power EPE/PEMC*, 2010, pp. S1-10–S1-17.

[19] R. Betz, R. Lagerquist, M. Jovanovic, T. J. E. Miller, and R. Middleton, "Control of synchronous reluctance machines," *IEEE Trans. Ind. Appl.*, vol. 29, no. 6, pp. 1110–1122, Nov./Dec.1993.

[20] J. Holtz and J. Quan, "Sensorless vector control of induction motors at very low speed using a nonlinear inverter model and parameter identification," *IEEE Trans. Ind. Appl.*, vol. 38, no. 4, pp. 1087–1095, Jul./Aug. 2002.

[21] L. Harnefors and H.-P. Nee, "A general algorithm for speed and position estimation of ac motors," *IEEE Trans. Ind. Electron.*, vol. 47, no. 1, pp. 77–83, Feb. 2000.

[22] P. Landsmann, C. Hackl, and R. Kennel, "Eliminating all machine parameters in encoderless predictive torque control without signal injection," in *Proc. IEEE IEMDC*, 2011, pp. 1259–1264.

Francois J. W. Barnard received the B.Eng. degree in electrical and electronic engineering and the M.Eng. degree in electrical engineering from Stellenbosch University, Stellenbosch, South Africa, in 2012 and 2014, respectively. His research interests include position sensorless control of reluctance synchronous machines.

Wikus Theo Villet received the B.Eng. and Ph.D. degrees in electrical and electronic engineering from Stellenbosch University, Stellenbosch, South Africa, in 2010 and 2014, respectively. His research interests include position sensorless control methods of reluctance synchronous machines.

Maarten J. Kamper (SM'08) received the M.Sc. (Eng.) and Ph.D. (Eng.) degrees from Stellenbosch University, Stellenbosch, South Africa, in 1987 and 1996, respectively.

Since 1989, he has been with the Department of Electrical and Electronic Engineering, Stellenbosch University, where he is currently a Professor of electrical machines and drives. His research interests include the design optimization and control of electrical machines, currently with the focus on wind generators and industrial and electric vehicle drives.

Prof. Kamper serves on the Steering Committee of the International Conference on Electrical Machines. He also serves as an Associate Editor for the Electric Machines Committee of the IEEE TRANSACTIONS ON INDUSTRY APPLICATIONS.